

# Numerical simulation of compressible flows with immersed boundaries using Discontinuous Galerkin methods

Bachelorarbeit von Simone Katharina Stange  
January 30, 2016



TECHNISCHE  
UNIVERSITÄT  
DARMSTADT

Fachbereich Maschinenbau

---

# Contents

<b>1. Motivation</b>	<b>1</b>
<b>2. Fundamentals</b>	<b>2</b>
2.1. Essential equations . . . . .	2
2.1.1. Equations of State . . . . .	2
2.1.2. Ideal Gas Law . . . . .	2
2.1.3. Navier-Stokes Equations . . . . .	3
2.2. Dimensionless Measures . . . . .	4
2.2.1. Non-dimensional Ideal Gas Law . . . . .	4
2.2.2. Dimensionless Navier-Stokes Equation . . . . .	5
<b>3. The Runge-Kutta Discontinuous Galerkin Method</b>	<b>6</b>
3.1. DG space discretization . . . . .	6
3.1.1. Weak formulation . . . . .	6
3.1.2. Numerical fluxes . . . . .	7
3.2. RK time discretization . . . . .	8
<b>4. Immersed Boundaries</b>	<b>12</b>
4.1. The DG Scheme with Immersed Boundaries . . . . .	12
4.2. RK Time Discretisation with Immersed Boundaries . . . . .	13
4.3. Cell Agglomeration . . . . .	13
<b>5. Parametric study of a flow around a cylinder</b>	<b>15</b>
5.1. Robustness study . . . . .	15
5.2. Convergence study of mesh size and polynomial degree . . . . .	17
<b>6. The viscous cylinder</b>	<b>19</b>
6.1. Theory . . . . .	19
6.1.1. The Laminar Steady Regime . . . . .	20
6.1.2. Laminar Vortex Shedding . . . . .	20
6.2. Simulations . . . . .	20
6.2.1. Steady State Simulations ( $Re < 40 - 50$ ) . . . . .	21
6.2.2. Unsteady Simulations ( $Re > 40 - 50$ ) . . . . .	24
<b>7. Discussion</b>	<b>28</b>
<b>8. Ehrenwörtliche Erklärung</b>	<b>VII</b>
<b>9. Declaration of Academic Integrity</b>	<b>VIII</b>
<b>List of Figures</b>	<b>IX</b>

---

<b>List of Tables</b>	<b>X</b>
<b>A. Anhang</b>	<b>XII</b>
A.1. Ein Anhang . . . . .	XII



---

# 1 Motivation

---

## 2 Fundamentals

---

### 2.1 Essential equations

---

In the following we will introduce the essential equations that form the basis of all results discussed in this thesis.

---

#### 2.1.1 Equations of State

---

First, I will enumerate the basic thermodynamic equations of state that describe the relations between the specific inner energy  $e$ , the local temperature  $T$ , the specific enthalpy  $\bar{h}$ , the pressure  $p = p(\rho, e)$ , the density  $\rho$  and the specific entropy  $s$ . Assuming that all material parameters are constant, we receive

$$e = c_v T \quad (2.1)$$

$$\bar{h} = c_p T = e + \frac{p}{\rho} \quad (2.2)$$

with the material parameters  $c_p$  and  $c_v$  as specific heat capacities at constant pressure and volume, respectively. Using these relations, we can define the heat capacity ratio

$$\gamma = \frac{c_p}{c_v} = \frac{\bar{h}}{e}. \quad (2.3)$$

As we will only be modelling standard air in this thesis, we will use  $\gamma = 1.4$ .

Another essential equation is the relation for the specific entropy

$$T ds = de + p d\rho^{-1}. \quad (2.4)$$

---

#### 2.1.2 Ideal Gas Law

---

The equations of state mentioned above are not yet complete as there is missing a law for the pressure  $p = p(\rho, e)$ . In this thesis we will confine ourselves to the ideal gas law for we are only

modelling standard air.

The ideal gas law is defined as

$$p = (\gamma - 1)\rho e \quad (2.5)$$

with  $\rho e \in \mathbb{R}^+$  denoting the inner energy.

The speed of sound is defined as

$$a = \sqrt{\left. \frac{\partial p}{\partial \rho} \right|_s}. \quad (2.6)$$

Using this definition combined with the ideal gas law and an equation for the change of entropy as can be read in **Mueller.2014** leads to the useful relations

$$a^2 = \gamma \frac{p}{\rho} \quad (2.7)$$

$$\frac{p}{\rho^\gamma} = \text{const.} \quad (2.8)$$

---

### 2.1.3 Navier-Stokes Equations

---

The compressible Navier-Stokes equations (CNS) in conservative forms read as

$$\frac{\partial \mathbf{U}}{\partial t} + \frac{\partial \mathbf{F}_i^c(\mathbf{U})}{\partial x_i} - \frac{\partial \mathbf{F}_i^v(\mathbf{U}, \nabla \mathbf{U})}{\partial x_i} = \mathbf{B}, \quad (2.9)$$

with the denotations  $\mathbf{U}$  as the conserved flow variables,  $\mathbf{F}_i^c$  and  $\mathbf{F}_i^v$  as the convective and viscous fluxes and  $\mathbf{B}$  as source terms:

$$\mathbf{U} = \begin{pmatrix} \rho \\ \rho v_j \end{pmatrix}, \quad \mathbf{F}_i^c = \begin{pmatrix} \rho v_i \\ \rho v_i v_j + p \delta_{ij} \\ v_i(\rho E + p) \end{pmatrix}, \quad \mathbf{F}_i^v = \begin{pmatrix} 0 \\ \tau_{ij} \\ \tau_{ij} + q_i \end{pmatrix}, \quad \mathbf{B} = \begin{pmatrix} 0 \\ \rho F_j \\ \rho F_j v_j + Q_i \end{pmatrix}. \quad (2.10)$$

In addition to the denotations in 2.1.1 we have  $F_j$  as body forces,  $Q_i$  as heat sources, the viscous stress tensor

$$\tau_{ij} = \mu \left[ \left( \frac{\partial v_i}{\partial x_j} + \frac{\partial v_j}{\partial x_i} \right) - \frac{2}{3} \frac{\partial v_k}{\partial x_k} \delta_{ij} \right] \quad (2.11)$$

with the dynamic viscosity  $\mu$  and the heat flux  $q_i$  modelled using Fourier's Law

$$q_i = k \frac{\partial T}{\partial x_i}. \quad (2.12)$$

### Euler Equations

Regarding only compressible inviscid flow, the viscous fluxes and the source terms dissolve ( $\mathbf{F}_i^v = \mathbf{B} = \mathbf{0}$ ) and the Navier-Stokes equations simplify to

$$\frac{\partial \mathbf{U}}{\partial t} + \frac{\partial \mathbf{F}_x^c(\mathbf{U})}{\partial x} + \frac{\partial \mathbf{F}_y^c(\mathbf{U})}{\partial y} = 0. \quad (2.13)$$

---

## 2.2 Dimensionless Measures

---

Dimensionless measures are very useful @TODO: wofür benötigt asterisk

$$t^* = \frac{V_\infty}{L_\infty} \cdot t, \quad x_i^* = \frac{1}{L} \cdot x_i, \quad v_i^* = \frac{1}{V_\infty} \cdot v_i, \quad \rho^* = \frac{1}{\rho_\infty} \cdot \rho, \quad p^* = \frac{1}{\rho_\infty V_\infty^2} \cdot p, \quad (2.14)$$

$$\mu^* = \frac{1}{\mu_\infty} \cdot \mu, \quad k^* = \frac{1}{k_\infty} \cdot k, \quad T^* = \frac{R}{V_\infty^2} \cdot T, \quad F_j^* = \frac{1}{g_\infty} \cdot F_j, \quad \rho E^* = \frac{1}{\rho_\infty V_\infty^2} \cdot \rho E, \quad (2.15)$$

$$Q_i^* = \frac{L}{V_\infty^3} \cdot Q \quad (2.16)$$

The dimensionless operators

$$\frac{\partial}{\partial t} = \frac{\partial t^*}{\partial t} \frac{\partial}{\partial t^*} = \frac{V_\infty}{L} \frac{\partial}{\partial t^*}, \quad (2.17)$$

$$\frac{\partial}{\partial x_i} = \frac{\partial x_i^*}{\partial x_i} \frac{\partial}{\partial x_i^*} = \frac{1}{L} \frac{\partial}{\partial x_i^*}, \quad (2.18)$$

$$\nabla = \frac{1}{L} \nabla^* \quad (2.19)$$

---

### 2.2.1 Non-dimensional Ideal Gas Law

---

In order to close the system of equations we need the ideal gas law in dimensionless form:

$$p^* = \rho^*(\gamma - 1)e^* \quad (2.20)$$

$$= (\gamma - 1) \left( \rho E^* - \frac{1}{2} \rho^* \mathbf{v}^{*2} \right). \quad (2.21)$$

---

### 2.2.2 Dimensionless Navier-Stokes Equation

---

Using the dimensionless measures and operators and defining the dimensionless relations

$$\text{Reynolds Number } \text{Re} = \frac{\rho_\infty V_\infty L}{\mu_\infty} \propto \frac{\text{inertia forces}}{\text{viscous forces}},$$

$$\text{Froude Number } \text{Fr} = \frac{V_\infty}{\sqrt{gL}} \propto \frac{\text{body inertia}}{\text{gravitational forces}},$$

$$\text{Prandtl Number } \text{Pr} = \frac{\mu_\infty c_p}{k_\infty} \propto \frac{\text{viscous diffusion rate}}{\text{thermal diffusion rate}},$$

we receive the dimensionless Navier-Stokes equations. As they only depend on dimensionless quantities we can drop the asterisk:

$$\frac{\partial \mathbf{U}}{\partial t} + \frac{\partial \mathbf{F}_i^c(\mathbf{U})}{\partial x_i} - \frac{\partial \mathbf{F}_i^v(\mathbf{U}, \nabla \mathbf{U})}{\partial x_i} = \mathbf{B} \quad (2.22)$$

with the dimensionless fluxes

$$\mathbf{F}_i^c = \begin{pmatrix} \rho v_i \\ \rho v_i v_j + p \delta_{ij} \\ v_i(\rho E + p) \end{pmatrix}, \quad \mathbf{F}_i^v = \frac{1}{\text{Re}} \begin{pmatrix} 0 \\ \tau_{ij} \\ \tau_{ij} v_j + \frac{\gamma}{\text{Pr}(\gamma - 1)} q_i \end{pmatrix}, \quad \mathbf{B} = \frac{1}{\text{Fr}^2} \begin{pmatrix} 0 \\ \rho F_j \\ \rho F_j v_j \end{pmatrix} + \begin{pmatrix} 0 \\ 0 \\ Q_j \end{pmatrix}. \quad (2.23)$$



---

## 3 The Runge-Kutta Discontinuous Galerkin Method

This thesis deals with a software that uses a Runge-Kutta Discontinuous Galerkin (RKDG) method for the numerical approximation of compressible flows. The RKDG method is split into the DG method for space discretization and the RK method as an explicit time discretization. By using an explicit time-marching algorithm, the parallelization is made much easier.

In the following sections we will study the DG and RK methods separately considering simple examples and using the same notation as in **Mueller.2014**

---

### 3.1 DG space discretization

---

First, we will study the Discontinuous Galerkin method which can be seen as combination of the Finite Volume and the Finite Element method.

As a simple example we will consider the scalar conservation law

$$\frac{\partial c}{\partial t} + \nabla \cdot \mathbf{f}(c) = 0 \quad (3.1)$$

for the concentration  $c = c(\mathbf{x}, t)$  with  $\vec{x} \in \Omega \subset \mathbb{R}^D$  and  $t \in \mathbb{R}_0^+$  and a smooth function  $\mathbf{f} : \mathbb{R} \rightarrow \mathbb{R}^D$  that also contains suitable initial and boundary conditions. **Mueller.2014**

---

#### 3.1.1 Weak formulation

---

Our first step of the DG method will be transferring the partial differential equation (3.1) into a weak formulation. Priorly to this we need a discretization  $\Omega_h$  of  $\Omega$  consisting of a tessellation of cells  $\{\mathcal{K}_i\}_{i=1,\dots,N}$ , where  $h$  represents a measure for the size of the cells. Each cell  $\mathcal{K}_i$  is of dimension  $D$  with an outward unit normal vector  $\mathbf{n}$ .

After having discretized our geometry, we now need a set of cell-local test functions  $\{\Phi_{i,j}\}_{j=1,\dots,M}$  with  $\Phi_{i,j} = \Phi_{i,j}(\mathbf{x}) : \mathbb{R}^D \rightarrow \mathbb{R}$  that forms the basis of polynomials  $P_{\mathcal{K}_i}(P)$  with the maximum degree  $P$ .

In order to obtain the weak formulation we will now multiply equation (3.1) by  $\Phi_{i,j}$ , integrate over a cell  $\mathcal{K}_i$  and then integrate by parts:

---


$$\begin{aligned}
\frac{\partial c}{\partial t} + \nabla \cdot \mathbf{f}(c) &= 0 \\
\frac{\partial c}{\partial t} \Phi_{i,j} + \nabla \cdot \mathbf{f}(c) \Phi_{i,j} &= 0 \\
\int_{\mathcal{K}_i} \frac{\partial c}{\partial t} \Phi_{i,j} dV + \int_{\mathcal{K}_i} \nabla \cdot \mathbf{f}(c) \Phi_{i,j} dV &= 0 \\
\int_{\mathcal{K}_i} \frac{\partial c}{\partial t} \Phi_{i,j} dV + \int_{\partial \mathcal{K}_i} (\mathbf{f}(c) \cdot \mathbf{n}) \Phi_{i,j} dA - \int_{\mathcal{K}_i} \mathbf{f}(c) \nabla \Phi_{i,j} dV &= 0.
\end{aligned}$$

Considering that the cell's surface  $\partial \mathcal{K}_i$  consists of internal or boundary edges  $\{\mathcal{E}_{i,e}\}_{e=1,\dots,E_i}$  we can rewrite the equation as

$$\int_{\mathcal{K}_i} \frac{\partial c}{\partial t} \Phi_{i,j} dV + \sum_{e=1}^{E_i} \int_{\mathcal{E}_{i,e}} (\mathbf{f}(c) \cdot \mathbf{n}) \Phi_{i,j} dA - \int_{\mathcal{K}_i} \mathbf{f}(c) \nabla \Phi_{i,j} dV = 0. \quad (3.2)$$

---

### 3.1.2 Numerical fluxes

---

As the concentration  $c$  is unknown, we need to introduce a modal approximation

$$c(\mathbf{x}, t) |_{\mathcal{K}_i} \approx \bar{c}(\mathbf{x}, t) |_{\mathcal{K}_i} = c_i(x, t) = \sum_{k=0}^M c_{i,k}(t) \Phi_{i,k}(\mathbf{x}) \quad (3.3)$$

with the Galerkin approach of identical Ansatz and test functions. For we do not enforce continuity on  $\mathcal{E}_{i,e}$  and thus

$$c_i |_{\mathcal{E}_{i,e}} =: c^- \neq c^+ := c_{n(i,e)} |_{\mathcal{E}_{i,e}} \quad (3.4)$$

we cannot simply insert the approximation into equation (3.2). Therefore we will introduce a monotone, Lipschitz continuous numerical flux function  $f = f(c^-, c^+, \mathbf{n}) : \mathbb{R}^{D+2} \rightarrow \mathbb{R}$  satisfying the consistency property

$$f(c^-, c^+, \mathbf{n}) = -f(c^-, c^+, -\mathbf{n}). \quad (3.5)$$

By including these definitions into (3.2) we receive

---


$$\int_{\mathcal{K}_i} \frac{\partial c_i}{\partial t} \Phi_{i,j} dV + \underbrace{\sum_{e=1}^{E_i} \int_{\mathcal{C}_{i,e}} f(c^-, c^+, \mathbf{n}) \Phi_{i,j} dA}_{=:(\mathbf{f}_i)_j} - \int_{\mathcal{K}_i} \mathbf{f}(c_i) \cdot \nabla \Phi_{i,j} dV = 0 \quad (3.6)$$

with the discrete operator  $\mathbf{f}_i = \mathbf{f}_i(t, \mathbf{c}_i) \in \mathbb{R}$ .

Some well-known examples of numerical fluxes contain **Cockburn**

- The Godunov flux
- The Engquist-Osher flux
- The Lax-Friedrichs flux
- The local Lax-Friedrichs flux
- The Roe flux with 'entropy flux',

whereby we will attend to the local Lax-Friedrichs or Rusanov flux, which is defined as

$$f(c^-, c^+, \mathbf{n}) = \frac{\mathbf{f}(c^-) + \mathbf{f}(c^+)}{2} \cdot \mathbf{n} - \frac{C_R}{2} (c^+ - c^-) \quad (3.7)$$

with the coefficient  $C_R$  based on a local stability criterion. In this thesis we will use an estimate based on the maximum local wave speed

$$C_R = \max(|\mathbf{u}^+ \cdot \mathbf{n}| + a^-, |\mathbf{u}^- \cdot \mathbf{n}| + a^+) \quad (3.8)$$

with  $u^\pm$  and  $a^\pm$  denoting the normal velocity and the local speed of sound at the edges. As the Rusanov flux has a high stability it will be used disregarding that it is prone to numerical diffusion.

---

## 3.2 RK time discretization

---

For we have studied the spatial discretization, we will now attend to the time discretization, using the Runge-Kutta method.

First of all, we need to reformulate equation (3.6) in order to achieve a system of coupled ODEs.

$$\int_{\mathcal{K}_i} \frac{\partial c_i}{\partial t} \Phi_{i,j} dV + \underbrace{\sum_{e=1}^{E_i} \int_{\mathcal{C}_{i,e}} f(c^-, c^+, \mathbf{n}) \Phi_{i,j} dA - \int_{\mathcal{K}_i} \mathbf{f}(c_i) \cdot \nabla \Phi_{i,j} dV}_{=:(\mathbf{f}_i)_j} = 0.$$

The first term of the equation above can be reformulated as

$$\begin{aligned} \int_{\mathcal{K}_i} \frac{\partial c_i}{\partial t} \Phi_{i,j} dV &= \int_{\mathcal{K}_i} \frac{\partial}{\partial t} \left( \sum_{k=0}^M c_{i,k}(t) \Phi_{i,k}(\mathbf{x}) \right) \Phi_{i,j} dV \\ &= \sum_{k=0}^M \frac{\partial c_{i,k}}{\partial t} \underbrace{\int_{\mathcal{K}_i} \Phi_{i,k} \Phi_{i,j} dV}_{=:(\mathbf{M}_i)_{k,j}} \\ &= \mathbf{M}_i \frac{\partial \mathbf{c}_i}{\partial t} \end{aligned}$$

thus leading to

$$\mathbf{M}_i \frac{\partial \mathbf{c}_i}{\partial t} + \mathbf{f}_i = 0 \quad (3.9)$$

with  $\mathbf{M}_i \in \mathbb{R}^{M,M}$  being a cell-local symmetric mass matrix associated with  $\mathcal{K}_i$ . As we have assumed an orthonormal basis  $\{\Phi_{i,j}\}_{j=1,\dots,M}$  thus reducing the mass matrix to the identity matrix  $I$ , the ODEs simplify to

$$\frac{\partial \mathbf{c}_i}{\partial t} + \mathbf{M}_i^{-1} \mathbf{f}_i = \mathbf{0} \quad (3.10)$$

$$\frac{\partial \mathbf{c}_i}{\partial t} + \mathbf{f}_i = \mathbf{0}. \quad (3.11)$$

Using an explicit RK method of Order  $S$  we can now advance this system of ODEs and calculate the new coefficients from

$$\mathbf{c}_i(t_1) = \mathbf{c}_i(t_0) - \Delta t \sum_{s=1}^S (\alpha)_s \mathbf{k}_s, \quad (3.12)$$

with a known solution at  $t_0$  to a new instant  $t_1$  and  $\Delta t = t_1 - t_0$ , where

$$\mathbf{k}_s = \mathbf{f}_i \left( t_0 + (\beta)_s \Delta t, \mathbf{c}_i(t_0) + \Delta t \sum_{t=1}^s (\Gamma)_{s,t} \mathbf{k}_t \right). \quad (3.13)$$

The coefficients  $\alpha \in \mathbb{R}^S$ ,  $\beta \in \mathbb{R}^S$  and  $\Gamma \in \mathbb{R}^S$  are specific for each RK method. The coefficients of the most common RK methods are displayed in the Butcher Tableaus in 3.2. They determine the stability and accuracy of the time integration scheme.

0					
$\beta_2$	$\Gamma_{21}$				
$\beta_3$	$\Gamma_{31}$	$\Gamma_{32}$			
$\vdots$	$\vdots$	$\vdots$	$\ddots$		
$\beta_s$	$\Gamma_{s1}$	$\Gamma_{s2}$	$\cdots$	$\Gamma_{s,s-1}$	
<hr/>					
	$\alpha_1$	$\alpha_2$	$\cdots$	$\alpha_{s-1}$	$\alpha_s$

**Table 3.1.:** Butcher tableau for the explicit RungeKutta method.

A well-known stability criterion according the explicit Euler time discretization for linear, hyperbolic PDEs, namely the Courant-Friedrichs-Lewy (CFL) criterion, restrains the temporal step-size  $\Delta t$ :

$$\Delta t \leq c_{CFL} \frac{h}{\underline{u}} \quad (3.14)$$

with  $\underline{u} \in \mathbb{R}^+$  denoting the largest propagation velocity and a positive constant  $c_{CFL} \leq 1$  depending on the applied spatial discretization procedure.

0				0				0				
				$\frac{1}{3}$	$\frac{1}{3}$			$\frac{1}{2}$	$\frac{1}{2}$			
	1	1		$\frac{2}{3}$	0	$\frac{1}{3}$		$\frac{1}{2}$	0	$\frac{1}{2}$		
<hr/>				<hr/>				<hr/>				
	1				$\frac{1}{4}$	0	$\frac{3}{4}$		$\frac{1}{6}$	$\frac{2}{6}$	$\frac{2}{6}$	$\frac{2}{6}$
<b>(a) Explicit Euler</b> (first order)				<b>(b) Trapezoidal rule</b> (second order)				<b>(c) Third order TVD</b> (third order)				
								<b>(d) Classical RK</b> (fourth order)				

**Table 3.2.:** Butcher Tableaus for different orders of RK

---

Concerning the Euler equations the largest propagation velocity is given by  $\underline{u} = \|\mathbf{u}\| + a$  and by taking the influence of the approximation order  $P$  into account we can use

$$\Delta t \leq \frac{c_{CFL}}{2P+1} \frac{h}{\|\mathbf{u}\| + a} \quad (3.15)$$

as a sufficiently accurate estimate for the stability criterion in this thesis.

## 4 Immersed Boundaries

In the following chapter we will study the DG method with immersed boundaries. IBMs are characteristic in the way of creating the calculation mesh as they do not rely on body fitted grids but on a level set function  $\varphi$  that cuts the cells into the physical and the void region. It therefore makes the mesh generation much easier, as it only needs a cartesian mesh and a function that approximates the level set. Brought along with the cartesian mesh, it is easily parallelisable, thus rendering it convenient for more complex structures that shall be computed on several processors.

### 4.1 The DG Scheme with Immersed Boundaries

We regard an implicit representation of an immersed boundary using the level set function  $\varphi$  that parts the calculation area  $\Omega_h$  into

the physical region  $\mathcal{A} = \{\vec{x} \in \Omega_h : \varphi(\vec{x}) > 0\}$ ,

the void region  $\mathcal{B} = \{\vec{x} \in \Omega_h : \varphi(\vec{x}) < 0\}$ ,

and the immersed boundary  $\mathcal{I} = \{\vec{x} \in \Omega_h : \varphi(\vec{x}) = 0\}$ .

In our next step we use the definitions above in 3.6 considering cell  $\mathcal{K}_i$  with the sub-domain  $\mathcal{A}_i = \mathcal{K}_i \cap \mathcal{A}$  and the surface  $\partial \mathcal{A}_i$ . As in cut cells the surface  $\partial \mathcal{A}_i$  consists not only of the edges  $\{\mathcal{E}_{i,e}^{\mathcal{A}}\}_{e=1,\dots,E} = \{\mathcal{E}_{i,e} \cap \bar{\mathcal{A}}_i\}_{e=1,\dots,E}$  but also of the boundary segment  $\mathcal{I}_i = \mathcal{K}_i \cap \mathcal{I}$ , the discrete weak formulation using an IBM follows as

$$\int_{\mathcal{A}_i} \frac{\partial c_i}{\partial t} \Phi_{i,j} dV + \sum_{e=1}^{E_i} \int_{\mathcal{E}_{i,e}^{\mathcal{A}}} f(c^-, c^+, \mathbf{n}) \Phi_{i,j} dA + \int_{\mathcal{I}_i} f(c^-, c^+, \mathbf{n}_{\mathcal{I}}) \Phi_{i,j} dA - \int_{\mathcal{A}_i} f(c_i) \cdot \nabla \Phi_{i,j} dV = 0 \quad (4.1)$$

with  $\mathbf{n}_{\mathcal{I}} = -\frac{\nabla \varphi}{\|\nabla \varphi\|}$ . In intersected cells the mass matrix is defined by

$$(\mathbf{M}_i)_{k,j} := \int_{\mathcal{A}_i} \Phi_{i,k} \Phi_{i,j} dV \quad (4.2)$$

and the discrete operator by

$$(\mathbf{f}_i)_j := \sum_{e=1}^{E_i} \int_{\mathcal{C}_{i,e}^{\mathcal{A}}} f(c^-, c^+, \mathbf{n}) \Phi_{i,j} dA + \int_{\mathcal{J}_i} f(c^-, c^+, \mathbf{n}_j) \Phi_{i,j} dA - \int_{\mathcal{A}_i} \mathbf{f}(c_i) \cdot \nabla \Phi_{i,j} dV. \quad (4.3)$$

The difficulty of the IBM lies in the correct evaluation of  $\mathcal{A}_i$  and  $\mathcal{J}_i$  and in the agglomeration of intersected cells with very small volume fractions

$$\text{frac}(\mathcal{A}_i) = \frac{\text{meas}(\mathcal{A}_i)}{\text{meas}(\mathcal{K}_i)} \quad (4.4)$$

as we will discuss in section 4.3.

---

## 4.2 RK Time Discretisation with Immersed Boundaries

---

In this thesis we use only explicit Euler time discretisation for immersed boundary problems:

$$\mathbf{c}_i(t_1) = \mathbf{c}_i(t_0) - \Delta t \mathbf{M}_i^{-1} \mathbf{f}_i(c). \quad (4.5)$$

Using IBMs we have to modify the stability criterion and therefore use the modified step restriction

$$\Delta t \leq \frac{c_{CFL}}{2P+1} \frac{\sqrt[D]{\text{meas}(\mathcal{A}_i)}}{\|\mathbf{u}\| + \alpha} \quad (4.6)$$

with a strong influence of the sub-cell  $\mathcal{A}_i$  with the smallest volume.

---

## 4.3 Cell Agglomeration

---

As can be seen in 4.6 the time step size is strongly restricted in cells with very small volume fractions. This leads to a very long calculation process thus rendering the method impractical. Therefore we need to agglomerate those small cells to larger ones using a cell agglomeration factor  $0 \leq \alpha \leq 1$ .

The cell agglomeration strategy relies on finding the source cells  $\{\mathcal{K}_s^{\text{src}}\}_{s=1,\dots,S}$  with  $\text{frac}(\mathcal{A}_i) \leq \alpha$  and agglomerating them to the neighboring cell with the highest volume fraction, namely target cell  $\mathcal{K}_s^{\text{tar}}$ .

For the neighboring cells are weakly coupled via fluxes, the basis  $\vec{\Phi}_i$  can be extended from the target cell into the source cell. Therefore the source cell can formally be deleted from



---

the discretisation mesh, reducing it to  $\{\mathcal{K}_s^{\text{agg}}\}_{i=1,\dots,N-S}$ . As can be found in @TODO: paper zitieren, it however does not reflect the actual implementation in Bounded Support Spectral Solver (BoSSS) which only requires few cell-local matrix-vector products per time-step, thus not affecting the parallel efficiency.

---

## 5 Parametric study of a flow around a cylinder

In the following chapter we will regard a flow at Mach 0.2 around a frictionless cylinder with adiabatic slip walls at changing parameters such as the polynomial degree, the mesh size and the position of the cylinder in order to validate BoSSS with immersed boundaries concerning robustness and convergence.

---

### 5.1 Robustness study

---

In the first study regarding the frictionless cylinder, we compare the absolute error of entropy for a polynomial degree from 1 to 3 along a shift of the centre point of the cylinder from  $-0.075$  to  $0.075$  at steps of  $0.015$ . By shifting the cylinder we can consider several cases where the cells would be cut differently and therefore cause different cell agglomerations. The cell agglomeration threshold is at a constant level of  $0.5$  in a mesh of  $32 \times 32$  cells. In this example we aim at proving the robustness of the solver as for each position of the cylinder the error of entropy should not vary too much thus making it independent of the way the border cells are cut.

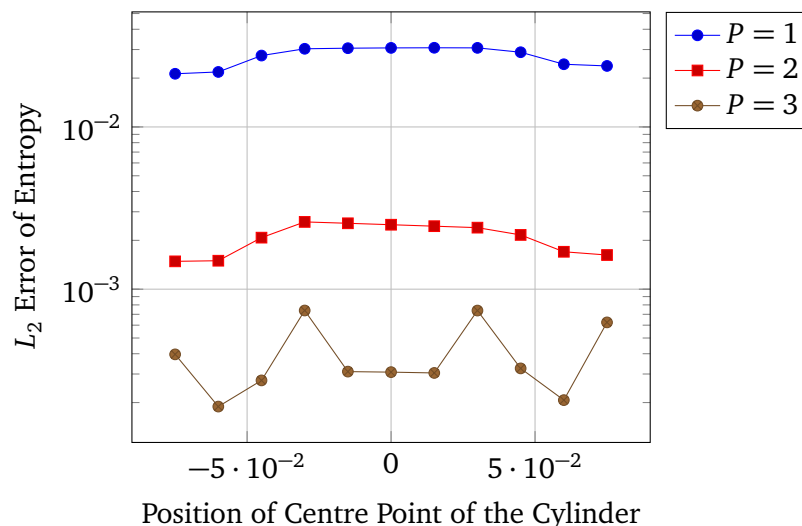


Figure 5.1.: Convergence Plot

As we look at the chart ??, first of all we will note that the absolute error of entropy decreases with increasing polynomial degree. As a higher polynomial degree implies a better approxima-

tion this can be explained very easily.

Secondly, we can observe that the error of entropy behaves roughly symmetrically to the ordinate. As we shifted the cylinder symmetrically this observation does not surprise us either.

Regarding the absolute error at a polynomial degree of 3, it is striking that this curve shows a much higher error difference compared to degrees 1 and 2. There are two peaks at a shift of  $\pm 0.03$ ; these discordant values were produced because the calculation stopped early. Unlike all other cases during this study, the calculation did not stop because the convergence criterion (change of error of entropy  $\leq 10^{-13}$ ) was reached but because the CFL number got invalid.

As these two values rather count as exceptions, we now consider two cases with a degree of 2 at the shifts of  $-0.06$  and  $-0.03$ .

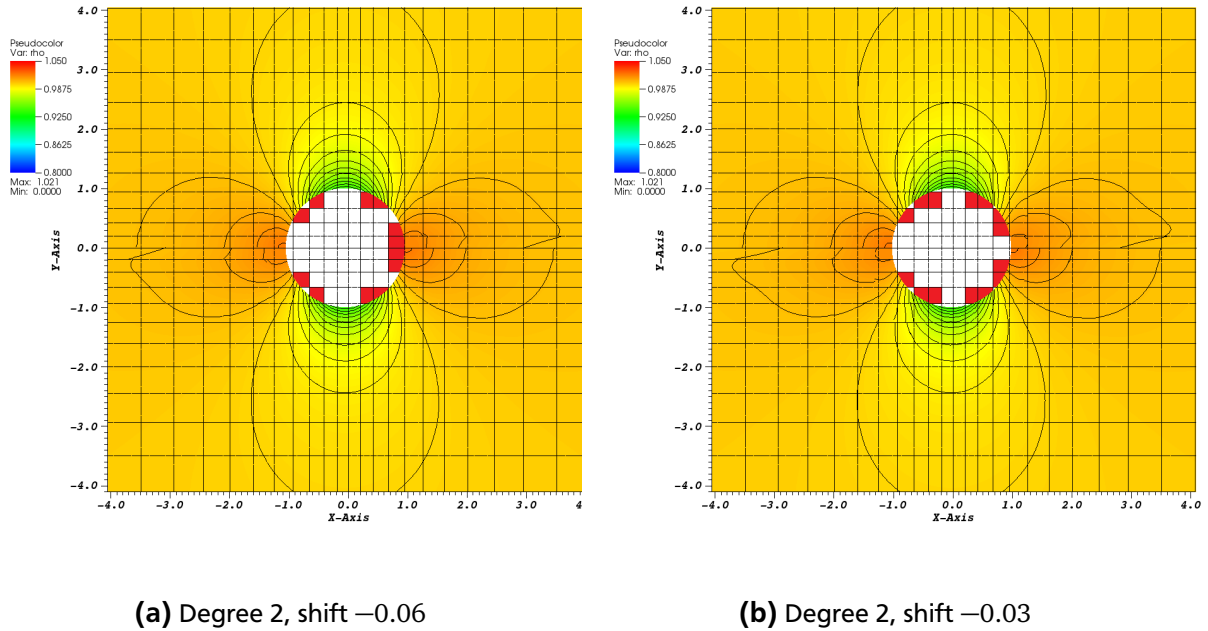


**Figure 5.2.:** Isolines of pressure

In figure 5.2 you can see the two mentioned cases with highlighted isolines of pressure and pseudocolored density. As only the upper half of the cylinder has been calculated, I reflected the results through the centre point of the cylinder. Therefore you can easily see that the results are not correct, as the flow before and after the obstacle should be identical. Furthermore you can see that in 5.2a the isolines are smoother than in 5.2b. In order to give an explanation for the higher error of entropy in 5.2b I highlighted the cells that should have been agglomerated in red. In the left case there are less agglomerated cells than in the right one, therefore there was a not so big agglomeration mistake made.

Except for the two discordant values at polynomial degree 3, the error of entropy changes very little for the different cases. We can therefore assume that the solver is good enough validated concerning the way the agglomerated cells influence the calculation. @TODO: cases nochmal rechnen um peaks wegzukriegen

## 5.2 Convergence study of mesh size and polynomial degree

In the second study we vary the mesh size of our geometry from  $32 \times 32$  by  $64 \times 64$  to  $128 \times 128$  cells. Additionally we also vary the polynomial degree from 0 to 4, consequently regarding fifteen cases in total.

Our aim is the verification of the convergence of the RKDGM based solver for the inviscid cylinder. Therefore we hope to achieve an experimental order of convergence that is near the optimal rate  $O(h^{P+1})$ . In chart ?? I compared the absolute error entropy to the mesh size logarithmically for each polynomial degree.

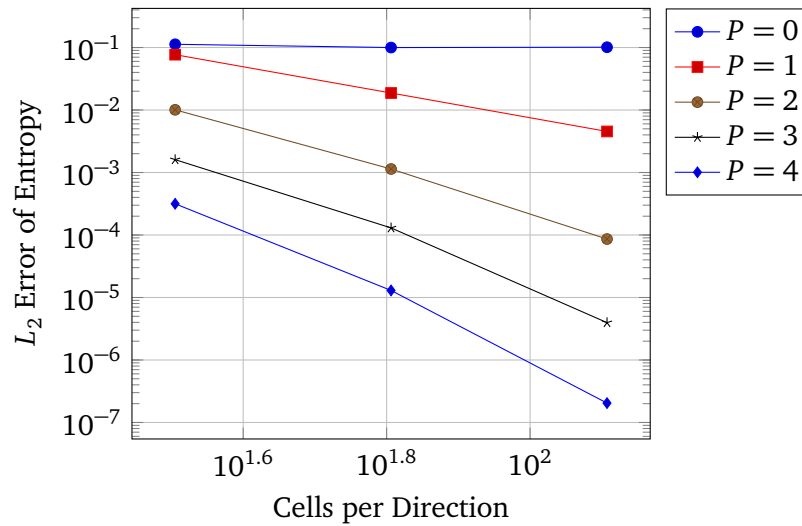
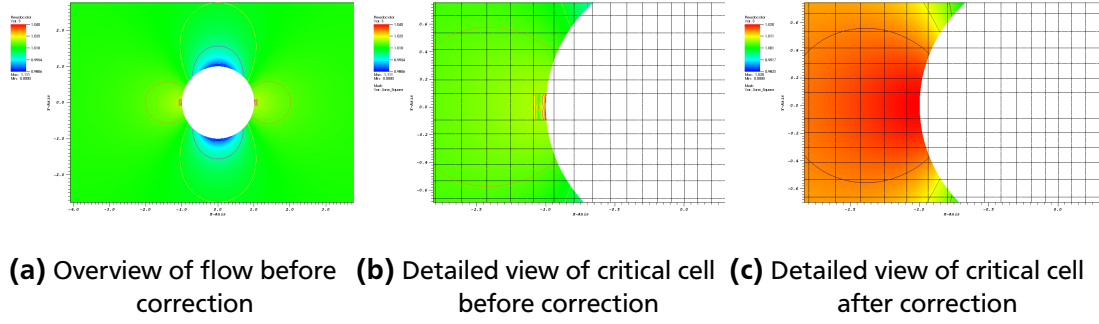


Figure 5.3.: Convergence Plot

As you can see in ?? each graph has a more or less constant gradient that is higher with increasing polynomial degree which is approximately of the order  $P+1$  as we hoped. Regarding the values of the  $128 \times 128$  mesh there are two discordant values: the case with mesh size  $128 \times 128$  and polynomial degree  $P=4$  did not terminate due to the error of entropy residual but because the CFL number could not be determined and therefore no value for the error of entropy was computed. The case for  $P=3$  has a disproportionately high value that is caused by two cells as can be seen in 5.4b. In order to correct the value I changed the *node count safety factor* from 2 to 5 which increases the robustness and therefore lets the calculation finish due to the residual. In 5.4 you can see the visualised flow of the inspected case with the critical spot where entropy is produced in 5.4b and the flow after the correction in 5.4c. Please remark that differently coloured entropy ranges had to be used in the two cases in order to point out the critical cell in 5.4b.



**Figure 5.4.:** Mesh size  $128 \times 128$ ,  $P = 3$

Concluding, we remark that the convergence behaves as desired with an order close to the optimal rate of  $O(h^{P+1})$ . Nevertheless to receive the correct result it should always be guaranteed that the calculation stops due to the residual rather than illegal values for momentum even if that means heightening the overall runtime by increasing the node count safety factor thus robustness.

## 6 The viscous cylinder

The flow around a viscous cylinder has been approached by many papers both analytically @TODO: wirklich? and numerically, e.g. @TODO: literatur, though very few numerical approaches use a Runge-Kutta Discontinuous Galerkin (RKDG) method combined with immersed boundaries. In order to verify the BoSSS code with immersed boundaries not only for the Euler equations as we did in chapter 5 but also for the viscous case we will now consider different Reynolds numbers for the steady and unsteady flow and compare our results to those of other studies.

### 6.1 Theory

The flow around a viscous cylinder can be divided into different sections depending on the flow specific Reynolds number. The first section applies for Reynolds numbers  $0 < Re < 40 - 50$  characterised by a laminar steady flow. In that regime a recirculation region with two symmetric vortices with opposite directions is comprised by the wake. The flow can be described using the wake separation length  $W^*$ .

The second section contains all other Reynolds number  $Re > 40 - 50$  and thus describes

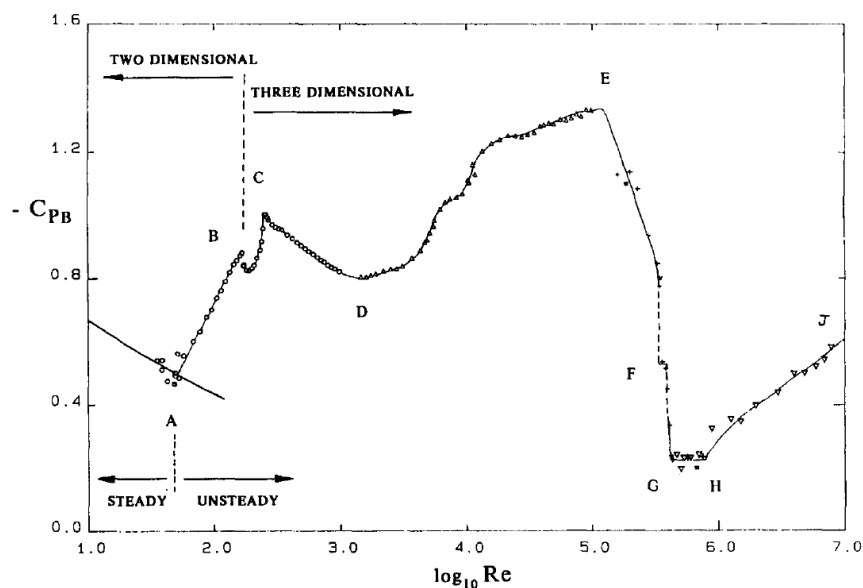


**Figure 6.1.:** Overview of Base Suction Coefficients over Reynolds Number @TODO: Quelle

the unsteady flow. It can be subdivided in several subsections:

---

$40 - 50 < Re < 190$  laminar vortex shedding,

$190 < Re < 260$  3-D wake-transition regime,

$260 < Re < 1000$  increasing disorder in the fine-scale three dimensionalities,

$1000 < Re < 200000$  shear layer transition regime,

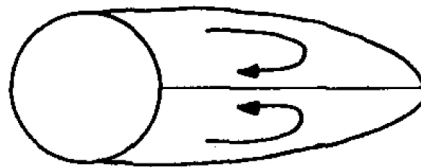
$200000 < Re$  critical transition, supercritical regime and post-critical regime.

As we will only discuss Reynolds numbers up to  $Re = 200$  the important phases for us are the laminar steady regime and the laminar vortex shedding. At around  $Re = 190$  the three dimensionality of the system has an incrementing influence on the flow; for we only analyse the 2-D model of the experiment we stop at  $Re = 200$  expecting slight deflection in our results.

---

### 6.1.1 The Laminar Steady Regime

---



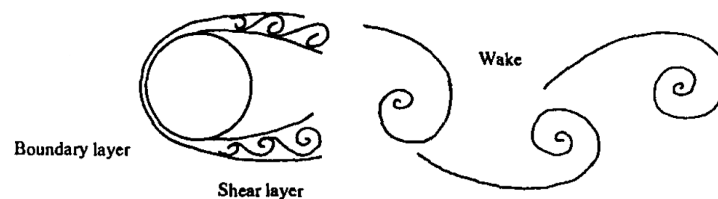
**STEADY WAKE**

**Figure 6.2.:** Recirculation Region @TODO: Quelle

---

### 6.1.2 Laminar Vortex Shedding

---



**UNSTEADY WAKE**

**Figure 6.3.:** Karmán Vortex Street @TODO: Quelle

---

## 6.2 Simulations

---

In this section we will compare the lift and drag coefficients at different Reynolds numbers and mesh sizes at a constant agglomeration threshold of 0.1, different polynomial degrees of 1, 2

and 3 and meshes of  $32 \times 32$ ,  $64 \times 64$  and  $128 \times 128$  cells. The different simulation properties will be abbreviated as DG + *polynomial degree* + MP + *number of cells per direction*, eg DG2MP64 for a simulation with polynomial degree 2 and  $64 \times 64$  cells.

The drag and lift coefficients  $C_D$  and  $C_L$  are defined as

$$C_D = \frac{d}{q_\infty L_\infty} \quad (6.1)$$

$$C_L = \frac{l}{q_\infty L_\infty} \quad (6.2)$$

with the dynamic pressure  $q_\infty = \frac{1}{2} \rho_\infty V_\infty^2$ . For we set  $L_\infty = \rho_\infty = V_\infty = 1$  in our boundary and initial conditions, we can assume

$$C_D = 2 \cdot d \quad (6.3)$$

$$C_L = 2 \cdot l, \quad (6.4)$$

with the drag and lift forces  $d$  and  $l$  provided from the calculation.

---

### 6.2.1 Steady State Simulations ( $Re < 40 - 50$ )

---

For the steady state simulations we can use the wake separation length  $W^*$  as an additional variable to compare to other simulations. It can be found from examining the velocity  $U$  at

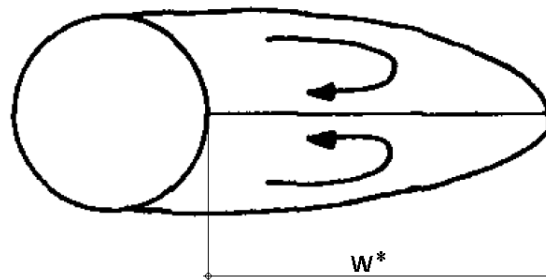


**Figure 6.4.:** Wake separation length @TODO: Quelle modified!

$y = 0$ ; the x-position where  $U$  changes its sign should be the end position of the wake.

---

Simulation at Reynolds Number 10

---



---

Simulation at Reynolds Number 20

---



---

Simulation at Reynolds Number 40

---



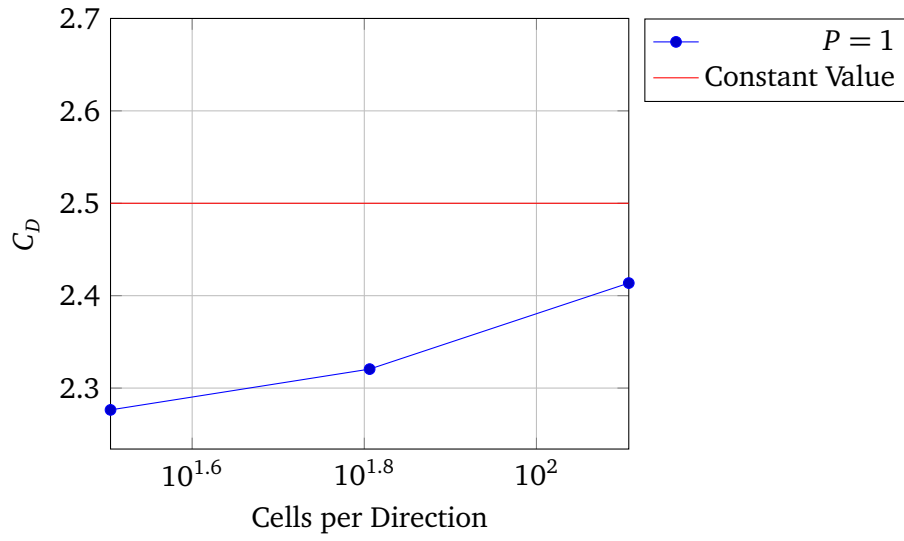


**Figure 6.5.:** Convergence Plot

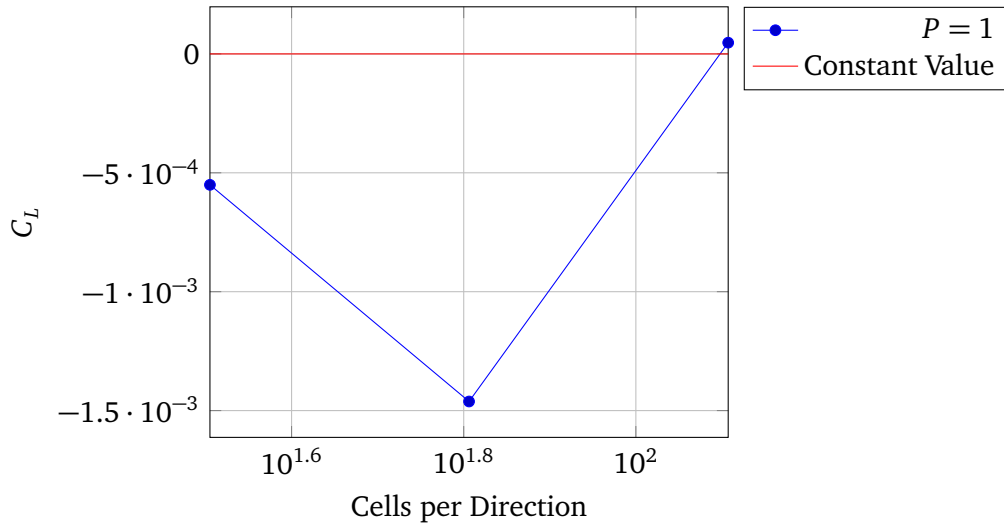


**Figure 6.6.:** Convergence Plot

Re = 20	Source	2D/3D	$W^*$	$C_D$
Numerical - Incompressible	Dennis et al [1970]	2D	0.94	2.05
	Forberg [1980]	2D	0.91	2.00
	Linnick et al. [2005]	2D	0.93	2.06
Experimental	Coutanceau et al. [1978]	-	0.93	-
	Tritton [1959]	-	-	2.09
Numerical Compressible	Brehm et al. [2015] (Ma = 0.1)	3D	0.96	2.02
	Ayers [2015]	2D	0.975	2.06
	<b>Present Results:</b>	2D	d	4

**Table 6.1.:** Comparison of Results for  $W^*$  and  $C_D$ , @TODO: modified Lawrence

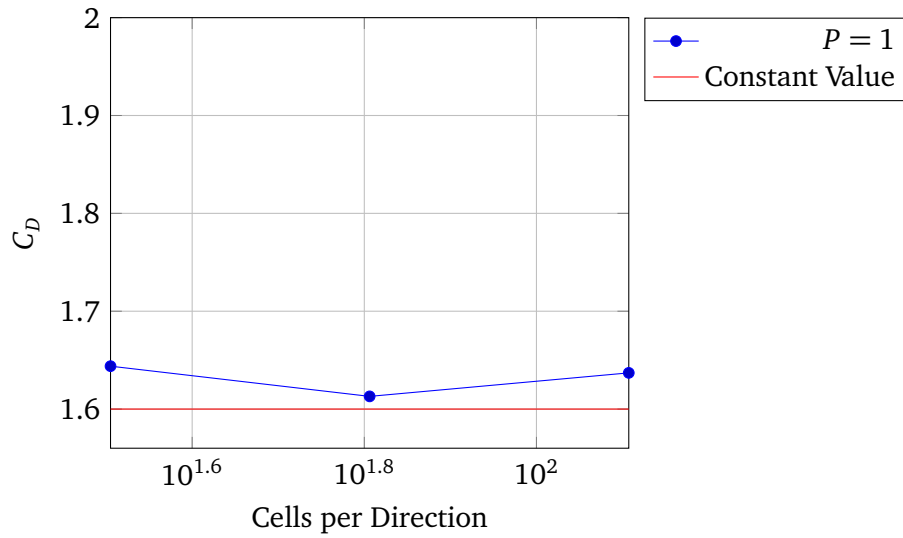


**Figure 6.7.:** Convergence Plot

Re = 40	Source	2D/3D	$W^*$	$C_D$
Numerical - Incompressible	Dennis et al [1970]	2D	2.35	1.52
	Forberg [1980]	2D	2.24	1.50
	Linnick et al. [2005]	2D	2.28	1.54
Experimental	Coutanceau et al. [1978]	-	2.13	-
	Tritton [1959]	-	-	1.59
Numerical Compressible	Brehm et al. [2015] (Ma = 0.1)	3D	2.26	1.51
	Ayers [2015]	2D	2.250	1.605
	<b>Present Results:</b>	2D	d	4

**Table 6.2.:** Comparison of Results for  $W^*$  and  $C_D$ , @TODO: modified Lawrence

---

### 6.2.2 Unsteady Simulations ( $Re > 40 - 50$ )

---

In order to compare the unsteady simulations we need the Strouhal number

$$St = \frac{f L_{\infty}}{V_{\infty}}. \quad (6.5)$$

As our initial and boundary conditions give  $V_{\infty} = L_{\infty} = 1$ , we can calculate  $St = f$  with  $f$  found from examining the oscillation of  $C_L$  over time.

---

#### Simulation at Reynolds Number 100

---

Re = 100	Source	2D/3D	$St$	$C_D$	$C_L$
Numerical - Incompressible	Gresho et al. [1984]	2D	0.18	1.76	-
	Linnick et al. [2005] ( $\lambda = 0.056$ )	2D	0.169	$1.38 \pm 0.010$	$\pm 0.337$
	Linnick et al. [2005] ( $\lambda = 0.023$ )	2D	0.169	$1.34 \pm 0.009$	$\pm 0.333$
	Persillon et al. [1998]	2D	0.165	1.253	-
	Saiki et al. [1996]	2D	0.171	1.26	-
	Persillon et al. [1998]	3D	0.164	1.240	-
	Liu et al. [1998]	3D	0.165	$1.35 \pm 0.012$	$\pm 0.339$
Experimental	Berger et al. [1972]	-	0.16-0.17	-	-
	Clift et al. [1978]	-	-	1.24	-
	Williamson [1996]	-	0.164	-	-
Numerical - Compressible	Brehm et al. [2015] ( $Ma = 0.1$ )	3D	0.165	$1.32 \pm 0.01$	$\pm 0.32$
	Ayers [2015]	2D	0.167	$1.371 \pm 0.011$	$\pm 0.333$
	<b>Present Results:</b>	2D	d	4	

**Table 6.3.:** Comparison of Results for  $St$ ,  $C_D$  and  $C_L$ , @TODO: modified Lawrence

---

#### Simulation at Reynolds Number 200

---

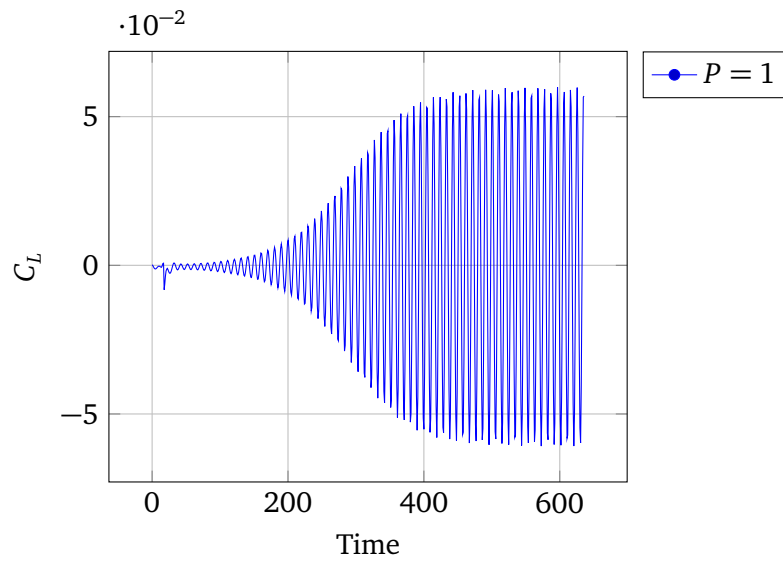


**Figure 6.8.: Convergence Plot**

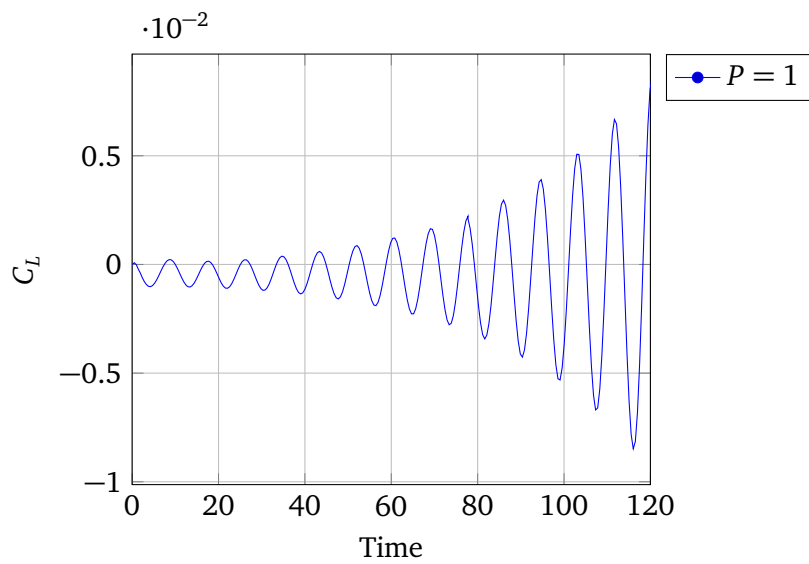


**Figure 6.9.: Convergence Plot**

Re = 100	Source	2D/3D	$St$	$C_D$	$C_L$
Numerical - Incompressible	Dennis et al [1970]	2D	0.94	2.05	
	Forberg [1980]	2D	0.91	2.00	
	Linnick et al. [2005]	2D	0.93	2.06	
Experimental	Coutanceau et al. [1978]	-	0.93	-	
	Tritton [1959]	-	-	2.09	
Numerical Compressible	Brehm et al. [2015] (Ma = 0.1)	3D	0.96	2.02	
	Ayers [2015]	2D	0.975	2.06	
	<b>Present Results:</b>	2D	d	4	

**Table 6.4.: Comparison of Results for  $W^*$  and  $C_D$ , @TODO: modified Lawrence**

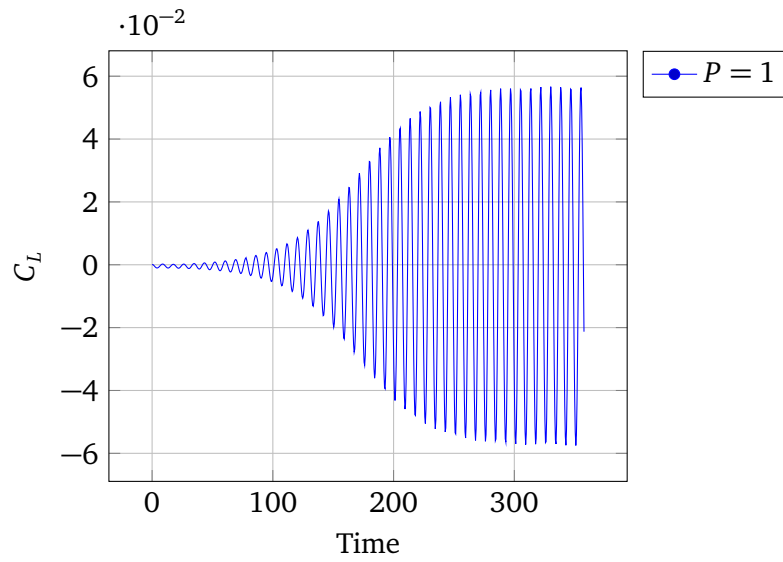


**Figure 6.10.:** Convergence Plot

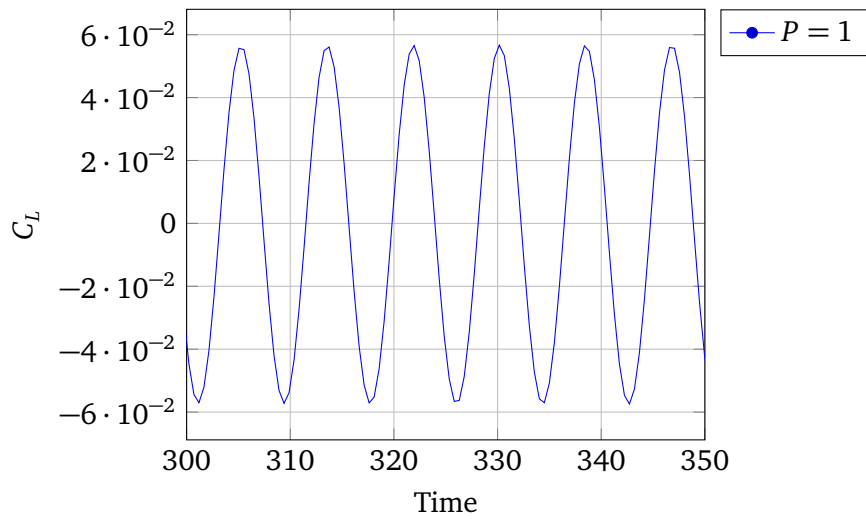


**Figure 6.11.:** Convergence Plot

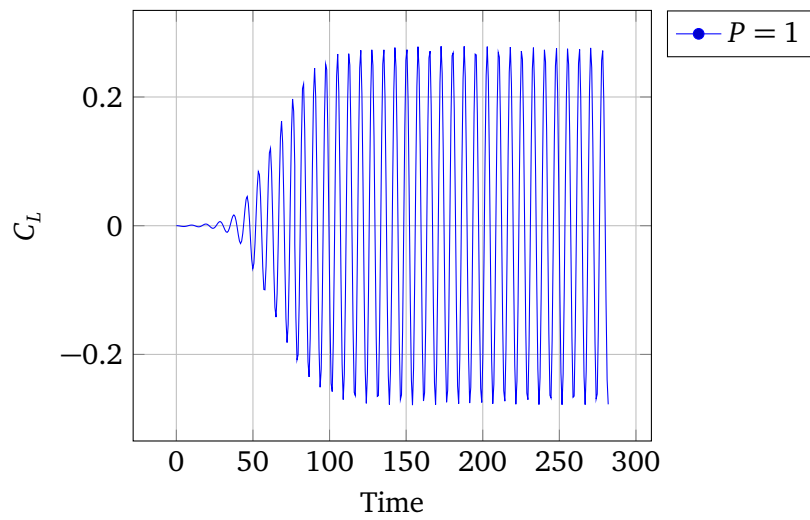


**Figure 6.12.:** Convergence Plot

---

## 7 Discussion



---

**Blomeke.2006**



---

## List of Figures

5.1. Convergence Plot . . . . .	15
5.2. Isolines of pressure . . . . .	16
5.3. Convergence Plot . . . . .	17
5.4. Mesh size $128 \times 128$ , $P = 3$ . . . . .	18
6.1. Overview of Base Suction Coefficients over Reynolds Number @TODO: Quelle . .	19
6.2. Recirculation Region @TODO: Quelle . . . . .	20
6.3. Karmán Vortex Street @TODO: Quelle . . . . .	20
6.4. Wake separation length @TODO: Quelle modified! . . . . .	21
6.5. Convergence Plot . . . . .	22
6.6. Convergence Plot . . . . .	22
6.7. Convergence Plot . . . . .	23
6.8. Convergence Plot . . . . .	25
6.9. Convergence Plot . . . . .	25
6.10. Convergence Plot . . . . .	26
6.11. Convergence Plot . . . . .	26
6.12. Convergence Plot . . . . .	27

---

## List of Tables

3.1. Butcher tableau for the explicit RungeKutta method. . . . .	10
3.2. Butcher Tableaus for different orders of RK . . . . .	10
6.1. Comparison of Results for $W^*$ and $C_D$ , @TODO: modified Lawrence . . . . .	22
6.2. Comparison of Results for $W^*$ and $C_D$ , @TODO: modified Lawrence . . . . .	23
6.3. Comparison of Results for $St$ , $C_D$ and $C_L$ , @TODO: modified Lawrence . . . . .	24
6.4. Comparison of Results for $W^*$ and $C_D$ , @TODO: modified Lawrence . . . . .	25





---

# A Anhang

---

## A.1 Ein Anhang

---